A Crucial Role of Rh Substituent Ion in Photoinduced Internal Electron Transfer and Enhanced Photocatalytic Activity of CdS–Ti$_{(5.2-x)/6}$Rh$_{x/2}$O$_2$ Nanohybrids

Jang Mee Lee, Hyung Bin Jin, In Young Kim, Yun Kyung Jo, Jung-Wook Hwang, Kang-Kyun Wang, Min Gyu Kim, Yong-Rok Kim,* and Seong-Ju Hwang*

The photocatalytic activity and photostability of CdS quantum dot (QD) can be remarkably enhanced by hybridization with Rh-substituted layered titanate nanosheet even at very low Rh substitution rate (<1%). Mesoporous CdS–Ti$_{(5.2-x)/6}$Rh$_{x/2}$O$_2$ nanohybrids are synthesized by a self-assembly of exfoliated Ti$_{(5.2-x)/6}$Rh$_{x/2}$O$_2$ nanosheets with CdS QDs. The partial substitution of Rh^{3+}/Rh^{4+} ions for Ti^{4+} ions in layered titanate is quite effective in enhancing an electronic coupling between hybridized CdS and titanate components via the formation of interband Rh 4d states. A crucial role of Rh substituent ion in the internal electron transfer is obviously evidenced from in situ X-ray absorption spectroscopy showing the elongation of (RhO) bond under visible light irradiation. This is the first spectroscopic evidence for the important role of substituent ion in the photoinduced electron transfer of hybrid-type photocatalyst. The CdS–Ti$_{(5.2-x)/6}$Rh$_{x/2}$O$_2$ nanohybrids show much higher photocatalytic activity for H$_2$ production and better photostability than do CdS and unsubstituted CdS–TiO$_2$ nanohybrid. This result is ascribable to the enhancement of visible light absorptivity, the depression of electron–hole recombination, and the enhanced hole curing of CdS upon Rh substitution. The present study underscores that the hybridization with composition-controlled inorganic nanosheet provides a novel efficient methodology to optimize the photo-related functionalities of semiconductor nanocrystal.

J. M. Lee, H. B. Jin, Dr. I. Y. Kim, Y. K. Jo,
Prof. S.-J. Hwang
Department of Chemistry and Nanoscience
Ewha Womans University
Seoul 03760, Korea
E-mail: hwangsju@ewha.ac.kr

H. B. Jin, J.-W. Hwang, Dr. K.-K. Wang, Prof. Y.-R. Kim
Department of Chemistry
College of Natural Sciences
Yonsei University
Seoul 03722, Korea
E-mail: yrkim@yonsei.ac.kr

Dr. M. G. Kim
Pohang Light Sources
Pohang 37673, Korea

1. Introduction

The hybridization of wide bandgap semiconductor with narrow bandgap semiconductor provides a powerful way to explore new efficient visible-light-active photocatalysts.[1–5] In this hybrid system, an electronic coupling between the component semiconductors is of prime importance in optimizing the photocatalytic activity of hybrid materials.[6–12] Taking into account the fact that the electronic coupling between the hybridized species occurs on their interface, the control of their crystal morphologies and surface structures is very crucial in designing strongly correlated hybrid system. Recently, we were successful in synthesizing highly efficient visible-light-active photocatalysts through the self-assembly between exfoliated titanate 2D nanosheet and

cadmium sulfide.[2] The subnanometer-level thickness of the exfoliated titanate nanosheet makes possible unusually strong electronic coupling with hybridized CdS, leading to the significant modification of electronic structure and the remarkable enhancement of photocatalytic activity upon the hybridization. Another merit of exfoliated metal oxide 2D nanosheets is the facile control of their chemical composition.[13,14] The application of chemically substituted layered metal oxide as a host material for exfoliation process allows us to synthesize the composition-tailored metal oxide nanosheets. Among many metal cations, the Rh^{3+}/Rh^{4+} ion is one of the most effective substituents for improving photocatalytic activity of titanium-oxide-based photocatalyst for visible-light-induced H_2 generation.[15] Such a positive effect of Rh substitution is attributable to the formation of impurity Rh 4d states in the bandgap of titanium oxide. In the hybrid system, the presence of Rh 4d interband states are supposed to promote an electronic interaction with the hybridized semiconductors through the provision of efficient pathways for internal electron transfer. This supposition gives an impetus to synthesize the Rh-substituted titanate nanosheets and to use them as building blocks for hybrid-type photocatalysts.[16] The Rh substitution for layered titanate nanosheet is expected to effectively depress the electron–hole recombination of CdS-layered titanate nanohybrids via the enhanced electronic coupling between the two components. The role of Rh substituent ions in the photoinduced internal electron transfer can be directly probed by element-selective in situ X-ray absorption spectroscopic (XAS) analysis under visible light illumination, providing critical insight for the effect of chemical substitution on the photo-related functionality of nanohybrid materials. At the time of the publication of the present study, however, we are aware of no reports on the synthesis of composition-controllable hybrid photocatalysts by adopting chemically substituted inorganic nanosheet as a building block and also a direct in situ spectroscopic analysis for the role of substituent ion in the photoinduced charge transfer.

In the present work, the electronic coupling and photocatalytic activity of self-assembled CdS-layered titanate nanohybrids can be optimized by the partial Rh substitution for layered titanate nanosheets. The evolutions of the crystal structure, porous structure, and electronic structure of the CdS-layered titanate nanohybrid upon Rh substitution are systematically investigated. The role of substituted Rh ions in the photoinduced electron transfer of the present nanohybrids is studied on the basis of in situ XAS analysis under the irradiation of visible light. The Rh-substituted CdS–$Ti_{(5.2−x)/6}Rh_{x/2}O_2$ nanohybrids are applied as photocatalysts for visible-light-induced H_2 generation to study the effects of Rh substitution on the photocatalytic activity and photostability of these hybrid materials.

2. Results and Discussion

2.1. Characterization of the Rh-Substituted Layered Titanates and Their Exfoliated Nanosheets

The crystal structures and morphologies of the Rh-substituted $K_{0.8}Ti_{(5.2−x)/3}Li_{(0.8−x)/3}Rh_xO_4$ materials are examined with powder X-ray diffraction (XRD) and field-emission scanning electron microscopy (FE-SEM) analyses. As presented in the top-left panel of **Figure 1**, regardless of Rh substitution, all of the pristine $K_{0.8}Ti_{(5.2−x)/3}Li_{(0.8−x)/3}Rh_xO_4$ materials display typical XRD pattern of layered titanate with lepidocrocite-type structure. Due to the larger size of Rh^{3+} ion (80.5 pm) than Ti^{4+} one (74.5 pm),[17] the increase of Rh content induces the distinct shift of Bragg reflections toward low angle side, indicating the expansion of unit cell volume upon the substitution of Ti with Rh (see Figure S1, Supporting Information). As illustrated in Figure S2 of the Supporting Information, all the pristine $K_{0.8}Ti_{(5.2−x)/3}Li_{(0.8−x)/3}Rh_xO_4$ materials commonly display 2D crystal morphology composed of layer-by-layer-stacked sheet-like crystallites, clearly demonstrating no marked morphological change of layered titanate upon Rh substitution. The homogeneous substitution of Rh for titanate is confirmed by energy-dispersive spectrometry (EDS)–elemental mapping analysis showing the uniform distribution of Rh element in the entire crystallites of layered titanate (Figure S2, Supporting Information).

The top-right panel of Figure 1 presents the diffuse reflection UV–vis spectra of the Rh-substituted $K_{0.8}Ti_{(5.2−x)/3}Li_{(0.8−x)/3}Rh_xO_4$ materials with $x = 0$–0.1 as well as the physical mixture of unsubstituted $K_{0.8}Ti_{1.73}Li_{0.27}O_4$ and 1% Rh_2O_3. In the spectrum of unsubstituted titanate, there is no distinct absorption peak in the wavelength region of $\lambda < 350$ nm, indicating the absence of interband state.
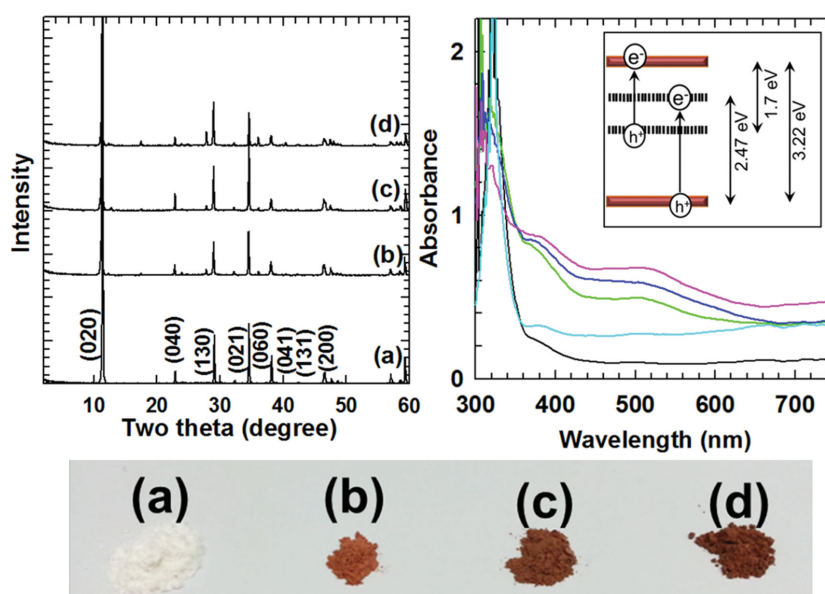

Figure 1. (Top-left) Powder XRD patterns, (top-right) diffuse reflectance UV–vis spectra, and (bottom) photographic images of the pristine $K_{0.8}Ti_{(5.2−x)/3}Li_{(0.8−x)/3}Rh_xO_4$ materials with $x =$ a) 0 (black), b) 0.025 (green), c) 0.05 (blue), and d) 0.1 (pink), and the reference physical mixture of unsubstituted $K_{0.8}Ti_{1.73}Li_{0.27}O_4$ and 1% Rh_2O_3 (cyan).

Conversely, the Rh substitution creates two distinct absorption peaks at ≈400 and ≈520 nm, reflecting the provision of visible light absorption ability. These spectral features provide strong evidence for the appearance of forbidden bands related to Rh^{3+} and Rh^{4+} ions between the bandgap of titanate,[14] as illustrated in the inset of Figure 1. The similar alteration of optical property upon the Rh substitution is also observed for the Rh-substituted $SrTiO_3$ material.[15] In comparison with the Rh-substituted $K_{0.8}Ti_{(5.2-x)/3}Li_{(0.8-x)/3}Rh_xO_4$ materials, the reference physical mixture of unsubstituted $K_{0.8}Ti_{1.73}Li_{0.27}O_4$ and 1% Rh_2O_3 displays much weaker absorption peaks at ≈400 nm as well as overall background absorption originating from black-colored Rh_2O_3. This strongly suggests much stronger influence of Rh substitution on the electronic structure of layered titanate compared with physical mixing. The remarkable modification of the electronic structure of layered titanate upon the Rh substitution is further evidenced by the distinct color change caused by the Rh substitution from white to reddish brown, see the bottom panel of Figure 1.

The photoluminescence (PL) spectra of the Rh-substituted $K_{0.8}Ti_{(5.2-x)/3}Li_{(0.8-x)/3}Rh_xO_4$ materials are measured with excitation wavelength of 380 nm to probe the effect of Rh substitution on the electron–hole recombination (see Figure S3, Supporting Information). The Rh substitution gives rise to remarkable depression of the PL signal of layered titanate, strongly suggesting the depression of the electron–hole recombination and the extension of the lifetimes of electrons and holes upon the Rh substitution. This is ascribable to the formation of interband states in the titanate component, as evidenced from the UV–vis results.

Although the increase of Rh content makes the PL signal weaker for lightly substituted materials, nearly identical PL intensity appears for both the heavily substituted materials with x = 0.05 and 0.1, strongly suggesting the saturation of Rh substitution effect. In the high Rh substitution rate, the beneficial effect of enhanced internal charge transfer seems to be compensated by the accompanying detrimental effect of recombination centers generated by the high-level Rh substitution.[18]

As presented in the top-left panel of **Figure 2**, the exfoliated colloidal nanosheets of Rh-substituted layered titanates retain the reddish brown color of the pristine materials, indicating the maintenance of the optical property of the host lattice upon exfoliation. The obtained colloidal suspensions of exfoliated $Ti_{(5.2-x)/6}Rh_{x/2}O_2$ nanosheets remain stable for longer than several months without notable precipitation. Regardless of the Rh substitution, the $Ti_{(5.2-x)/6}Rh_{x/2}O_2$ suspensions possess negative zeta potentials of −35—45 mV, underscoring the anionic nature of these exfoliated nanosheets, see the top-right panel of Figure 2. The Rh substitution makes greater the negative charge of layered titanate nanosheets, which can be interpreted as a result of the partial replacement of Ti^{4+} ions with lower valent Rh^{3+}/Rh^{4+} ions. As illustrated in the bottom-left panel of Figure 2, the transmission electron microscopy (TEM) images of the exfoliated $Ti_{(5.2-x)/6}Rh_{x/2}O_2$ nanosheets clearly demonstrate that all of the present nanosheets display 2D sheet-like morphology with faint contrast, confirming the exfoliation of layered titanate into very thin nanosheets. The formation of Rh-substituted layered $Ti_{(5.2-x)/6}Rh_{x/2}O_2$ nanosheet is further confirmed by the EDS–elemental mapping analysis showing the
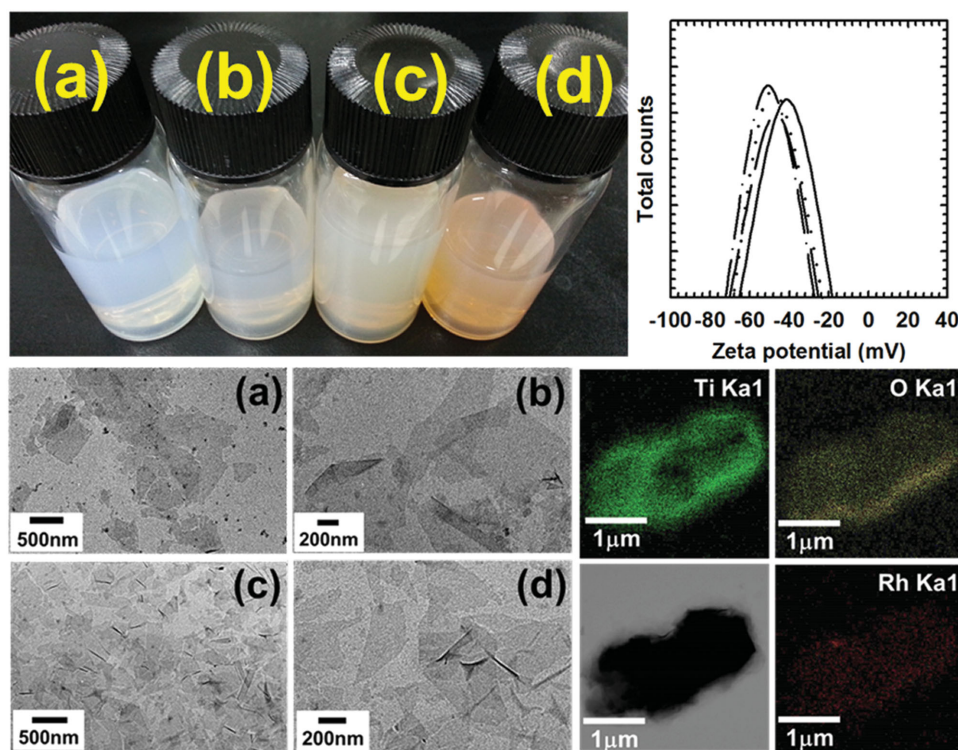

Figure 2. (Top-left) Photographic images, (top-right) zeta potential plots, (bottom-left) TEM images, and (bottom-right) EDS–elemental maps of the colloidal $Ti_{(5.2-x)/6}Rh_{x/2}O_2$ nanosheets with x = a) 0 (solid line), b) 0.025 (dashed line), c) 0.05 (dotted line), and d) 0.1 (dash-doted line).
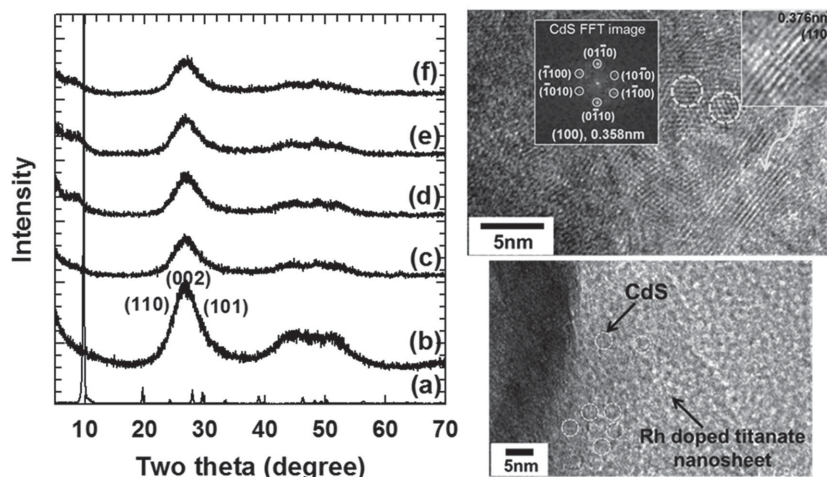
Figure 3. (Left) Powder XRD patterns of a) the protonated titanate, b) CdS QDs, and the self-assembled CdS–Ti$_{(5.2-x)/6}$Rh$_{x/2}$O$_2$ nanohybrids with x = c) 0, d) 0.025, e) 0.05, and f) 0.1. (Right) HR-TEM and FFT data of the CdS–Ti$_{(5.2-x)/6}$Rh$_{x/2}$O$_2$ nanohybrid.

suggesting the good dispersion of exfoliated titanate nanosheets in the present nanohybrid materials without distinct phase separation. The immobilization of CdS QDs on the surface of Ti$_{(5.2-x)/6}$Rh$_{x/2}$O$_2$ nanosheets is cross-confirmed by TEM analysis. As illustrated in the right panel of Figure 3, the obtained nanohybrid is composed of the nanoscale mixture of two different domains. Clear lattice fringes corresponding to the CdS and Ti$_{(5.2-x)/6}$Rh$_{x/2}$O$_2$ species are observed, underscoring the hybridization between these two nanospecies. From the interplanar distances, the observed lattice planes can be indexed as the (100) plane of hexagonal CdS lattice and the (110) plane of orthorhombic titanate lattice. The coexistence of CdS and Ti$_{(5.2-x)/6}$Rh$_{x/2}$O$_2$ nanosheets provides strong evidence for the intimate hybridization in the CdS–Ti$_{(5.2-x)/6}$Rh$_{x/2}$O$_2$ nanohybrid. The anchoring of CdS QDs is further evidenced by fast Fourier transform (FFT) simulation for the CdS domains showing distinct hexagonal diffraction spots of CdS phase.

homogeneous distribution of Rh, Ti, and O elements in the entire part of present nanosheet, as presented in the bottom-right panel of Figure 2.

2.2. Powder XRD and TEM Analyses for CdS–Ti$_{(5.2-x)/6}$Rh$_{x/2}$O$_2$ Nanohybrids

The CdS–Ti$_{(5.2-x)/6}$Rh$_{x/2}$O$_2$ nanohybrids are synthesized by electrostatically derived hybridization between the anionic Ti$_{(5.2-x)/6}$Rh$_{x/2}$O$_2$ nanosheets and the cationic CdS QD with the particle size of ≈25 Å, as illustrated in the left panel of **Figure 3**.[19] The left panel of Figure 3 illustrates the powder XRD patterns of the self-assembled CdS–Ti$_{(5.2-x)/6}$Rh$_{x/2}$O$_2$ nanohybrids, as compared with those of the protonated titanate and CdS QD. All of the present nanohybrids commonly show broad XRD features of CdS QD at 2θ = ≈25°–30°, confirming the immobilization of CdS QDs on the surface of layered titanate nanosheets. Conversely, no XRD peaks of layered titanate are discernible, strongly

2.3. FE-SEM/EDS and Elemental Analyses for CdS–Ti$_{(5.2-x)/6}$Rh$_{x/2}$O$_2$ Nanohybrids

The left panel of **Figure 4** illustrates the FE-SEM images of the present CdS–Ti$_{(5.2-x)/6}$Rh$_{x/2}$O$_2$ nanohybrids. All of the present nanohybrids display highly porous morphology formed by the house-of-cards-type stacking of layered crystallites, indicating the effective formation of mesoporous structure with expanded surface area via the exfoliation-reassembling process. The nanoscale hybridization between CdS and Ti$_{1-x}$Rh$_x$O$_2$ in the nanohybrids is further confirmed by EDS–elemental mapping analysis, see the right panel of Figure 4. All of the CdS–Ti$_{(5.2-x)/6}$Rh$_{x/2}$O$_2$ nanohybrids demonstrate the uniform distribution of Cd, S, Ti, and Rh
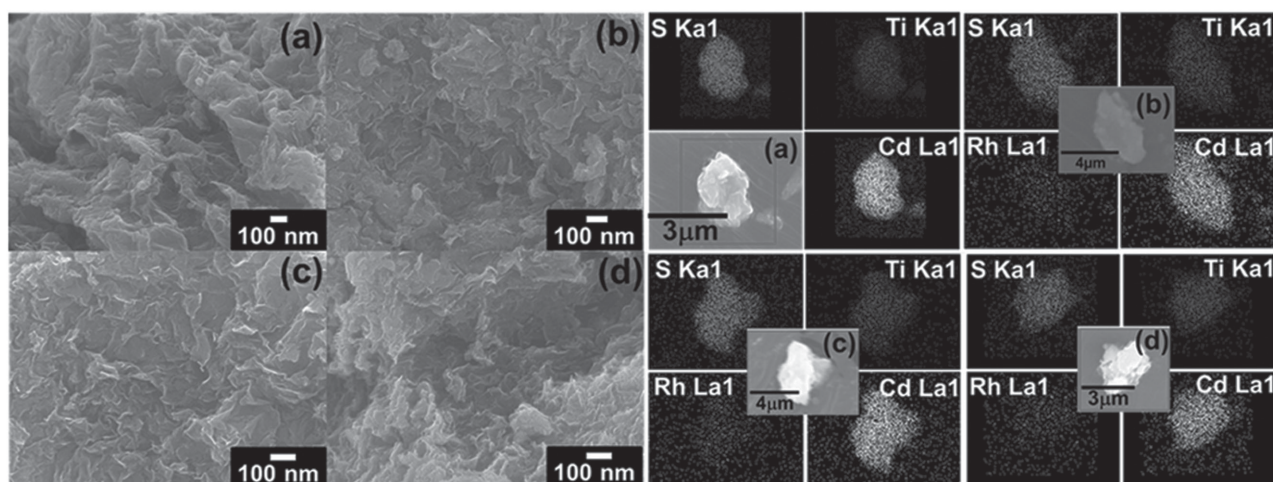

Figure 4. (Left) FE-SEM images and (right) EDS maps of the self-assembled CdS–Ti$_{(5.2-x)/6}$Rh$_{x/2}$O$_2$ nanohybrids with x= a) 0, b) 0.025, c) 0.05, and d) 0.1.

elements in entire parts of the samples, highlighting the formation of self-assembled CdS–Ti$_{(5.2-x)/6}$Rh$_{x/2}$O$_2$ lattice. According to inductively coupled plasma (ICP) spectrometry, all the CdS–Ti$_{(5.2-x)/6}$Rh$_{x/2}$O$_2$ nanohybrids possess similar Cd/(Ti±Rh) ratio of 2.0, which is smaller than the initial ratio of the reactants. The gradual increase of Rh content in the present CdS–Ti$_{(5.2-x)/6}$Rh$_{x/2}$O$_2$ nanohybrids occurs with the change of Rh content in the pristine materials; the Rh contents of the present CdS–Ti$_{(5.2-x)/6}$Rh$_{x/2}$O$_2$ nanohybrids with $x = 0.025$ (0.48%), 0.05 (0.77%), and 0.1 (1.92%) are determined to be 0.30, 0.57, and 1.75%, respectively.

2.4. N$_2$ Adsorption–Desorption Isotherm Analysis

The surface areas and pore structures of the present materials are examined using N$_2$ adsorption–desorption isotherm analysis, see the left panel of **Figure 5**. The pristine layered titanate materials show only a negligible adsorption of N$_2$ molecules whereas the hybridization with CdS QD leads to the remarkable enhancement of N$_2$ adsorption, strongly suggesting the expansion of surface area. All of the CdS–Ti$_{(5.2-x)/6}$Rh$_{x/2}$O$_2$ nanohybrids induce significant N$_2$ adsorption at low pp$_0^{-1}$ region with distinct hysteresis at pp$_0^{-1} > 0.6$, reflecting the formation of micropores and mesopores. The observed isotherms and hysteresis behaviors of the present nanohybrid materials are classified as Brunauer–Deming–Deming–Teller (BDDT)-type I and IV shape of isotherms and a H3-type hysteresis loop in the IUPAC classification.[20] This feature of isotherm indicates the formation of the open slit-shaped capillaries with very wide bodies and narrow short necks. According to the fitting analysis using the Brunauer–Emmett–Teller (BET) equation, all the CdS–Ti$_{(5.2-x)/6}$Rh$_{x/2}$O$_2$ nanohybrids possess expanded surface area of ≈151 m^2 g^{-1} for $x = 0$, ≈207 m^2 g^{-1} for $x = 0.025$, ≈178 m^2 g^{-1} for $x = 0.05$ and ≈172 m^2 g^{-1} for $x = 0.1$, which are much greater than those of the pristine K$_{0.8}$Ti$_{(5.2-x)/3}$Li$_{(0.8-x)/3}$Rh$_x$O$_4$ materials (≈1 m^2 g^{-1}). This result provides strong evidence for the merit of exfoliation–reassembling in creating the porous structure. The slight increase of the surface area upon the Rh substitution reflects that Rh-substituted nanohybrid possesses more loosely packed stacking structure of exfoliated nanosheets. This is attributable to the increase of negative charge of Ti$_{(5.2-x)/6}$Rh$_{x/2}$O$_2$ nanosheets upon Rh substitution, leading to the enhanced repulsion among the restacked nanosheets. According to the calculation of the pore size distribution of the nanohybrids with the Barrett–Joyner–Halenda (BJH) method, all of the self-assembled nanohybrids have mesopores with an average diameter of ≈3–4 nm, see the right panel of Figure 5. This mesopore is formed by the house-of-cards-type stacking of layered crystallites, as evidenced by the FE-SEM analysis (the left panel of Figure 4).

2.5. Ti K-Edge, Rh K-Edge, and Cd K-Edge XAS and Rh 3d XPS Analyses

The chemical bonding natures of the pristine K$_{0.8}$Ti$_{(5.2-x)/3}$Li$_{(0.8-x)/3}$Rh$_x$O$_4$ and the CdS–Ti$_{(5.2-x)/6}$Rh$_{x/2}$O$_2$ nanohybrids are examined with X-ray absorption near-edge structure (XANES) analysis at Ti K-edge, Rh K-edge, and Cd K-edge (see Figure S4, Supporting Information). In the Ti K-edge region, there is no significant difference in the edge positions of the pristine K$_{0.8}$Ti$_{(5.2-x)/3}$Li$_{(0.8-x)/3}$Rh$_x$O$_4$ and the CdS–Ti$_{(5.2-x)/6}$Rh$_{x/2}$O$_2$ nanohybrids, indicating no marked change in tetravalent Ti oxidation state upon the Rh substitution and the hybridization with CdS.[21] For all the present spectra, there are four pre-edge peaks P$_1$, P$_2$, P$_2'$, P$_3$ corresponding to the dipole-forbidden 1s → 3d transitions, whereas three features A, B, and C related to dipole-allowed 1s → 4p transitions appear in main-edge region.[22,23] In both the regions, all the pristine K$_{0.8}$Ti$_{(5.2-x)/3}$Li$_{(0.8-x)/3}$Rh$_x$O$_4$ materials display nearly identical spectral features to their nanohybrids with CdS, which are characteristic of lepidocrocite-type layered titanate structure. This observation clearly demonstrates the maintenance of original lepidocrocite-type titanate structure upon the Rh substitution and the hybridization with CdS.[2]

In the Rh K-edge XANES region, all the pristine K$_{0.8}$Ti$_{(5.2-x)/3}$Li$_{(0.8-x)/3}$Rh$_x$O$_4$ and the CdS–Ti$_{(5.2-x)/6}$Rh$_{x/2}$O$_2$ nanohybrids display nearly identical edge position, which is slightly higher than that of the reference Rh$_2$O$_3$, indicating the mixed oxidation state of Rh^{3+}/Rh^{4+} ions in these materials. The overall spectral features of the nanohybrids are almost the same as those of the pristine materials, underscoring negligible effect of CdS hybridization on the local atomic arrangement of substituted Rh ions in the titanate.

The local structure of substituted Rh ion in the present nanohybrids is quantitatively investigated using Rh K-edge extended X-ray absorption fine structure (EXAFS) analysis. According to the EXAFS fitting analysis, the substituted Rh ions in the CdS–Ti$_{(5.2-x)/6}$Rh$_{x/2}$O$_2$ nanohybrid are coordinated by oxygen ligands with the (Rh—O) bond distance
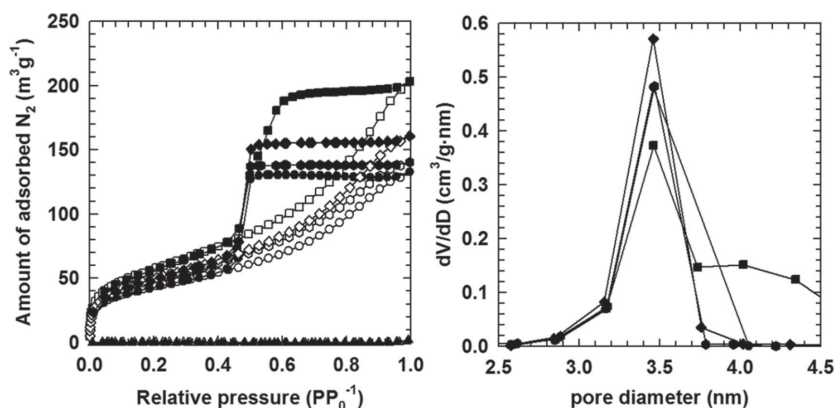

Figure 5. (Left) N$_2$ adsorption–desorption isotherms and (right) pore size distributions of a) the pristine K$_{0.8}$Ti$_{(5.2-x)/3}$Li$_{(0.8-x)/3}$Rh$_x$O$_4$ (triangle) and the CdS–Ti$_{(5.2-x)/6}$Rh$_{x/2}$O$_2$ nanohybrids with $x=$ b) 0 (circles), c) 0.025 (squares), d) 0.05 (diamonds), and e) 0.1 (hexagons). The open and close symbols represent the adsorption and the desorption data, respectively.

of 2.00 Å. The obtained (Rh—O) bond distance of the present nanohybrid is somewhat shorter than that of the trivalent reference Rh_2O_3 (2.025 Å), reflecting the higher mixed $Rh^{3\pm}/Rh^{4\pm}$ oxidation state in the former compound. To accurately determine the coordination number of Rh ion, the amplitude reduction factor is obtained from the EXAFS fitting analysis for the reference Rh_2O_3 and used for the calculation of the coordination number of Rh ion in the present nanohybrid. The coordination number of 5.3 is obtained for the present nanohybrid, confirming the stabilization of Rh ion in octahedral Ti site of layered titanate lattice. The mixed oxidation state of $Rh^{3\pm}/Rh^{4\pm}$ in the present nanohybrids is further evidenced by Rh 3d X-ray photoelectron spectroscopy (XPS) analysis (see Figure S5, Supporting Information). Both of the present $CdS–Ti_{(5.2-x)/6}Rh_{x/2}O_2$ nanohybrid and the reference Rh_2O_3 commonly show two XPS peaks corresponding to Rh $3d_{5/2}$ and Rh $3d_{3/2}$ states. In comparison with the reference Rh_2O_3 having the $Rh^{3\pm}$ oxidation state, the $CdS–Ti_{(5.2-x)/6}Rh_{x/2}O_2$ nanohybrid displays higher binding energies for both the XPS peaks, confirming the mixed oxidation state of $Rh^{3\pm}/Rh^{4\pm}$ ions in this material, which is in good agreement with the XANES result.

The Cd K-edge XANES results demonstrate nearly identical spectral feature and edge position for the present $CdS–Ti_{(5.2-x)/6}Rh_{x/2}O_2$ nanohybrids and the reference CdS, reflecting the maintenance of CdS upon the hybridization with layered titanate. The observed spectral features of the present nanohybrids are obviously distinguishable from that of CdO, which allows us to rule out the possible oxidation of CdS QD upon the hybridization with the $Ti_{(5.2-x)/6}Rh_{x/2}O_2$ nanosheets.

to longer wavelength upon the Rh substitution, confirming the enhancement of visible light absorptivity. The resulting optical absorption edge of the present nanohybrids is located in longer wavelength region than that of the precursor CdS, which can be interpreted as a result of the strong electronic coupling between small CdS QDs and subnanometer-thick titanate nanosheets.[2] In this strongly coupled hybrid system, an electron transfer can occur from the valance band (VB) of CdS to the conduction band (CB) and/or indirect bands of titanate, leading to the shift of optical absorption edge more suitable for visible light harvesting. The Rh-substituted $CdS–Ti_{(5.2-x)/6}Rh_{x/2}O_2$ nanohybrids display absorption edge in longer wavelength than do the Rh-free nanohybrid and the precursor CdS QD, underscoring the usefulness of the combination of Rh substitution and CdS hybridization in tailoring the electronic structure of photocatalyst material.

The right panel of Figure 6 represents the PL spectra of the $CdS–Ti_{(5.2-x)/6}Rh_{x/2}O_2$ nanohybrids, as compared with the reference CdS QD. The strong PL signal of CdS QD becomes remarkably depressed by the hybridization with the $Ti_{(5.2-x)/6}Rh_{x/2}O_2$ nanosheet, indicating the depression of electron–hole recombination and the elongation of lifetime of charge carriers. This is a result of strong electronic coupling between CdS and layered titanate nanosheets. Additionally the hybridization with Rh-substituted titanate leads to the further decrease of the PL signal of CdS compared with that with unsubstituted titanate. This observation provides strong evidence for the enhancement of the electronic coupling between CdS and layered titanate upon the partial substitution of Ti ions with Rh ions.

2.6. Diffuse Reflectance UV–Vis and PL Spectroscopic Analyses

The diffuse reflectance UV–vis spectra of the $CdS–Ti_{(5.2-x)/6}Rh_{x/2}O_2$ nanohybrids are plotted in the left panel of **Figure 6**, as compared with that of CdS QD. Similarly to the pristine-layered titanate, the $CdS–Ti_{(5.2-x)/6}Rh_{x/2}O_2$ nanohybrids also induce the shift of optical absorption edge

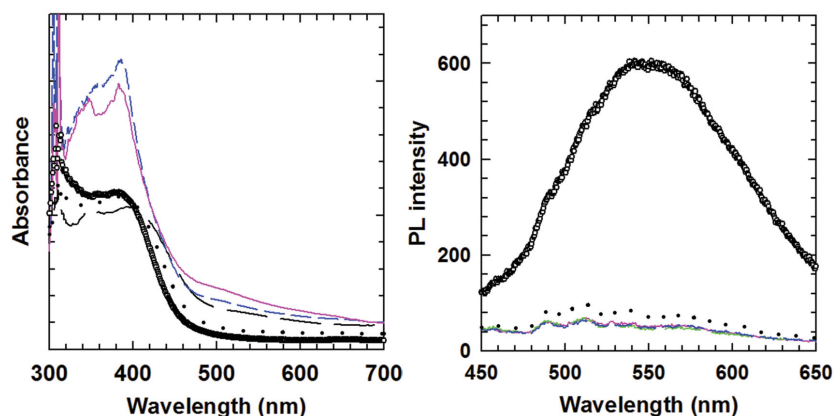### 2.7. In Situ Rh K-Edge EXAFS Analysis under the Irradiation of Visible Light

The role of substituted Rh ion in the photoinduced internal charge transfer in the present $CdS–Ti_{(5.2-x)/6}Rh_{x/2}O_2$ nanohybrid is investigated with in situ Rh K-edge EXAFS analysis under the irradiation of visible light. The top-left and top-right panels of **Figure 7** illustrate the k^3-weighted Rh K-edge EXAFS oscillations of the $CdS–Ti_{(5.2-x)/6}Rh_{x/2}O_2$ nanohybrid with $x = 0.05$ and their Fourier transform (FT) data before and after the illumination of visible light, respectively. Although both the present EXAFS oscillations show nearly identical spectral features, visible light irradiation induces a minute but distinct decrease of oscillation wavelength, indicating the lengthening of (Rh—O) bond distance and the decrease of Rh oxidation state.[24] Similarly, the visible light-irradiated nanohybrid displays a distinct shift of the first FT peaks corresponding to the (Rh—O) shell toward longer R side, confirming the elongation of (Rh—O) bond distance and the reduction of Rh oxidation state. As listed in **Table 1**, the increase of (Rh—O) bond distance after the
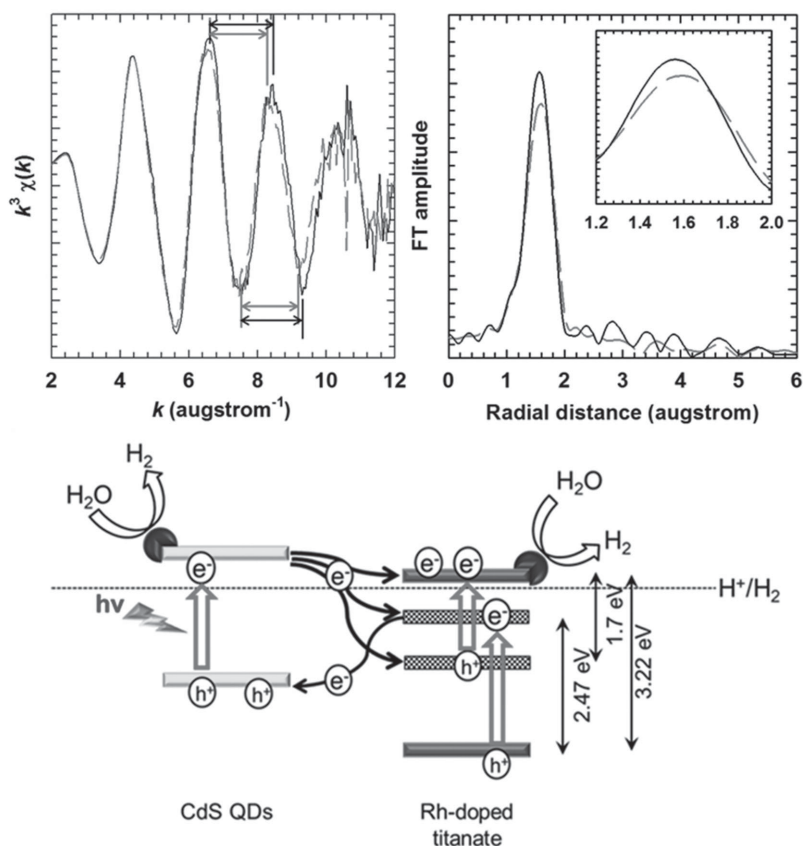

Figure 6. (Left) Diffuse reflectance UV–vis and (right) PL spectra of the $CdS–Ti_{(5.2-x)/6}Rh_{x/2}O_2$ nanohybrids with $x = 0$ (dot), 0.025 (long dash), 0.5 (short dash), and 0.1 (solid), and reference CdS QD (circle).

ponents and an intimate coupling between them, the irradiation of visible light can induce electron excitations from VB/interband state to CB/interband state in both the components. The reduction of Rh ion caused by visible light irradiation provides clear evidence for the enhanced electronic coupling between the two components upon the Rh substitution, promoting the photoexcited electron transfer from the CB of CdS to the CB/interband states of the Rh-substituted titanate. The presence of Rh 4d interband states facilitates this internal electron transfer of the present nanohybrids. The resulting depression of electron–hole recombination is responsible for the further depression of the PL signal of CdS-layered titanate nanohybrid upon the Rh substitution (Figure 6).

2.8. Test of Photocatalytic Activity

Figure 8 presents the time-dependent production of H_2 gas by the visible-light-illuminated suspensions of the CdS–Ti$_{(5.2-x)/6}$Rh$_{x/2}$O$_2$ nanohybrids, as compared with those by the pristine K$_{0.8}$Ti$_{(5.2-x)/3}$Li$_{(0.8-x)/3}$Rh$_x$O$_4$ materials and CdS. Even without the deposition of Pt cocatalyst, all of the present nanohybrids possess fairly high photocatalytic activity for the visible light ($\lambda > 420$ nm)-induced H_2 generation.[25] The CdS–Ti$_{(5.2-x)/6}$Rh$_{x/2}$O$_2$ nanohybrids are much more photocatalytically active than the precursors CdS QDs and the pristine K$_{0.8}$Ti$_{(5.2-x)/3}$Li$_{(0.8-x)/3}$Rh$_x$O$_4$ materials, underscoring the unique advantage of the hybridization between exfoliated titanate nanosheets and CdS QDs with strong electronic coupling. As can be seen from the band structure model in the bottom panel of Figure 7, the Rh substitution leads to the enhancement of visible light absorption but not all the absorbed phonon energy contributes to H_2 production. Thus, the observed enhancement of photocatalytic activity upon Rh substitution is attributable mainly to the depression of electron–hole recombination caused by the promoted internal electron transfer rather than to the enhanced visible light absorption. For comparison, the physical mixture of CdS and layered Ti$_{(5.2-x)/6}$Rh$_{x/2}$O$_2$ was also prepared by mixing of two precursors with the Cd/(Ti+Rh) ratio of 2.5. This material is much less photocatalytically active compared with the present nanohybrid, confirming the crucial importance of strong electronic coupling achieved by the hybridization between subnanometer-thick titanate nanosheets and very small CdS QDs. As can be seen clearly from Figure 8, the Rh-substituted materials display markedly higher photocatalytic activity than do the unsubstituted homologue, highlighting the usefulness of the Rh-substituted titanate nanosheet as a building block for synthesizing highly efficient photocatalyst materials via the fine-tuning of electronic coupling. The
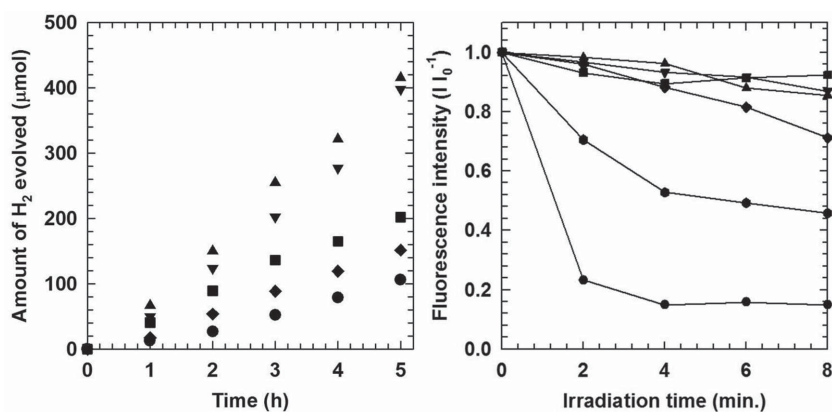

Figure 7. (Top-left) In situ Rh K-edge EXAFS spectra and (top-right) their Fourier transforms (FT) of the self-assembled CdS–Ti$_{(5.2-x)/6}$Rh$_{x/2}$O$_2$ nanohybrid with $x = 0.1$ before (solid) and after (dahsed line) the illumination of visible light. (Bottom) Schematic model for the band structures of CdS–Ti$_{(5.2-x)/6}$Rh$_{x/2}$O$_2$ nanohybrids. The inset of Fourier transform shows the enlarged view of RhO bond distance in longer R region.

illumination of visible light is cross-confirmed by non-linear curve fitting analysis for the present EXAFS data. This observation clearly demonstrates a significant role of substituted Rh ions in the photoinduced internal charge transfer of the present nanohybrid. To the best of our knowledge, this is the first direct spectroscopic evidence for the crucial role of substituent ions in the photoinduced electron transfer in hybrid-type photocatalyst.

On the basis of the present results of UV–vis, PL, and in situ Rh K-edge EXAFS analyses, the band structure of the present CdS–Ti$_{(5.2-x)/6}$Rh$_{x/2}$O$_2$ nanohybrid can be described in the bottom panel of Figure 7. Taking into account the small bandgap separations of CdS and Rh-substituted titanate com-

Table 1. Results of non-linear least-squares curve fittings for the Rh K-edge EXAFS spectra of the CdS–Ti$_{(5.2-x)/6}$Rh$_{x/2}$O$_2$ nanohybrid with $\underline{x} = 0.05$ before and after the illumination of visible light. The curve fitting analysis was performed for the range of 0.767–R–2.393 Å and 2.70–k–11.80 Å^{-1}, and 0.736–R–2.332 Å and 2.75–k–11.30 Å^{-1}.

Sample	Bond	CN	R [Å]	σ^2 [$10^{-3} \times$ Å^2]	ΔE [eV]
Before	Rh—O	6	2.00	4.758	3.5
After	Rh—O	6	2.02	5.734	4.7

Figure 8. (Left) Visible light ($\lambda > 420$ nm)-induced H_2 production and (right) photostability tests of the CdS–Ti$_{(5.2-x)/6}$Rh$_{x/2}O_2$ nanohybrid with $x = 0$ (diamonds), 0.025 (squares), 0.05 (triangles), and 0.1 (inverse triangles), with the reference CdS QDs (circles) and P25 TiO$_2$–CdS (hexagons).

quantum yield of the CdS–Ti$_{(5.2-x)/6}$Rh$_{x/2}O_2$ nanohybrid with $x = 0.05$ is estimated to be 5.7% at 420 nm. Although this value is slightly lower than the previously reported data for Pt-loaded CdS–TiO$_2$,[26–28] no loading of Pt cocatalyst on the present materials strongly suggests the validity of the present synthetic strategy for exploring high-performance photocatalyst materials.

The photostabilities of the CdS–Ti$_{(5.2-x)/6}$Rh$_{x/2}O_2$ nanohybrids are also investigated with time-dependent PL spectroscopy. As plotted in the right panel of Figure 8, the precursor CdS QD experiences a significant decrease of PL intensity to ≈85% of the original intensity after irradiation, indicating poor photostability of CdS QD. The hybridization of CdS QD with P25 TiO$_2$ nanoparticle leads to only a slightly enhancement of photostability (≈56% depression), indicating the limited improvement of photostability upon the hybridization with TiO$_2$ nanoparticle. Of prime importance is that the PL depression is negligible for all the present CdS–Ti$_{(5.2-x)/6}$Rh$_{x/2}O_2$ nanohybrids (<≈10% decrease), highlighting the remarkable improvement of the photostability of CdS QDs upon the coupling with 2D titanate nanosheets. This is attributable to the removal of hole in CdS by electrons transferred from titanate nanosheet. Among the present nanohybrids, the Rh-substituted materials display much weaker depression of PL signal than does the unsubstituted homologue, underscoring the beneficial effect of Rh substitution in enhancing the photostability of the present nanohybrid. Even for the extended illumination for a longer period of 1 h, all the present CdS–Ti$_{(5.2-x)/6}$Rh$_{x/2}O_2$ nanohybrids commonly still display good retention of PL intensity of ≈80%, ≈84%, and ≈90% for $x = 0.025$, 0.05, and 0.1 (see Figure S6, Supporting Information). All of the materials show a saturation of PL decay after 40 min, confirming the significant improvement of the photostability of CdS upon the hybridization. The enhanced photostability of CdS in the present nanohybrid is further confirmed by the measurement of the leaching of Cd^{2+} ion during the photocatalyst test. In comparison with the pristine CdS QDs showing a significant leaching of Cd ion (52.6 ppm), much weaker dissolution of Cd ions (17.2 ppm) occurs for the CdS–Ti$_{(5.2-x)/6}$Rh$_{x/2}O_2$ nanohybrid with $x = 0.05$. The observed improvement of pho-

tostability can be understood as a result of the enhanced internal charge transfer caused by the formation of interband Rh 4d state, leading to the efficient curing of hole in CdS component.

The effects of photocatalytic test on the crystal structure, crystal morphology, and chemical composition of the present CdS–Ti$_{(5.2-x)/6}$Rh$_{x/2}O_2$ nanohybrids are investigated with powder XRD, FE-SEM, EDS–elemental mapping, and XPS analyses (see Figure S7 and S8, Supporting Information). Even after the photocatalytic reaction, the present nanohybrids still retain their original XRD patterns, confirming the maintenance of nanohybrid structure. These CdS–Ti$_{(5.2-x)/6}$Rh$_{x/2}O_2$ nanohybrids subjected to the photocatalyst test still possess their original house-of-cards-type stacking structure, underscoring negligible influence of visible light on their morphology. Similarly the coexistence of Ti$_{(5.2-x)/6}$Rh$_{x/2}O_2$ nanosheets and CdS QDs in the photoreacted nanohybrids is evidenced by the EDS analysis. Additionally the Rh 3d XPS analysis provides clear evidence for the maintenance of the mixed oxidation state of Rh$^{3\pm}$/Rh$^{4\pm}$ upon the photocatalyst test.

3. Conclusion

The hybridization with composition-controlled titanate nanosheet is quite powerful not only in optimizing the electronic coupling between hybridized CdS and layered titanate components but also in improving the photocatalytic activity and photostability of CdS QD. The partial substitution of Ti^{4+} with Rh^{3+}/Rh^{4+} gives rise to the depression of bandgap energy and electron–hole recombination, which is attributable to the enhancement of electronic coupling between CdS and layered titanate caused by the formation of interband Rh 4d states. A clear spectroscopic evidence on the crucial role of Rh substituent ion in the photoinduced electron transfer of the present hybrid photocatalyst is obtained for the first time from the in situ EXAFS analysis under visible light irradiation. The CdS–Ti$_{(5.2-x)/6}$Rh$_{x/2}O_2$ nanohybrids are fairly photocatalytically active for visible-light-induced H_2 generation, which is superior to the precursor CdS QD and non-substituted CdS-layered titanate nanohybrid. The remarkable increase of visible light photocatalytic activity upon the Rh substitution is ascribable to the enhancement of electronic coupling between the hybridized components. This finding provides strong evidence for the usefulness of composition control in optimizing the photocatalytic activities of nanosheet-based hybrid materials. Although the CdS–Ti$_{(5.2-x)/6}$Rh$_{x/2}O_2$ nanohybrids show high photocatalytic activity only for the half-cell reaction, i.e., the visible-light-induced H_2 generation in the presence of sacrificial agent, the present materials can be applied as useful component for the Z-scheme-based photocatalyst systems efficient for H_2 production or CO_2 reduction. Also these materials can be used

as efficient electrode materials for water photosplitting in photoelectrochemical cell, since the loading of electrochemical potential makes it possible to control the band position of the electrode material. Taking into account the fact that many energy-related functionalities of inorganic materials are strongly dependent on their electronic structures, there is a wide room to improve diverse energy-related functionalities of nanohybrid materials via the chemical substitution for the component nanosheet and the resulting control of electronic structure. In one instance, the cationic substitution of metal oxide nanosheet leads to the change of CB position, whereas the replacement of oxygen with other anion makes possible the tuning of VB position.[29,30] Thus the co-substitution of cation and anion can provide a powerful way to tailor the electronic structure of metal oxide nanosheet and hence to optimize their energy-related functionalities. Our current project is the application of the present substitution strategy for exploring novel nanosheet-based hybrid materials with excellent energy-related functions such photocatalysts, electrocatalysts, and electrodes for photovoltaic.

4. Experimental Section

Preparation: The Rh-substituted layered titanates of $K_{0.8}Ti_{(5.2-x)/3}Li_{(0.8-x)/3}Rh_xO_4$ with $x = 0$, 0.025, 0.05, and 0.1 were prepared by sintering the stoichiometric mixture of K_2CO_3, Li_2CO_3, TiO_2, and Rh_2O_3 at 800 °C for 1 h and 1000 °C for 20 h in ambient atmosphere. The protonated derivatives were obtained by the reaction of the pristine $K_{0.8}Ti_{(5.2-x)/3}Li_{(0.8-x)/3}Rh_xO_4$ with 1 M HCl aqueous solution for 72 h. The exfoliated $Ti_{(5.2-x)/6}Rh_{x/2}O_2$ nanosheets were synthesized by the intercalation of tetrabutylammonium (TBA) cation into the protonated material at room temperature.[31,32] A small amount of unexfoliated particle was separated from the colloidal suspension with high-speed centrifugation at 10 000 rpm for 10 min. The positively charged CdS QD was prepared by the previously reported solution-based method,[33] in which cadmium acetate dehydrate, 2-mercaptoethylamine hydrochloride, and thioacetamide were reacted at 40 °C for 5 h and then at 60 °C for 5 h under vigorous stirring. The powdery amine-modified CdS QD was restored from the solution by the repeated dispersion in water and precipitation by the addition of isopropyl alcohol. The CdS–$Ti_{(5.2-x)/6}Rh_{x/2}O_2$ nanohybrids were synthesized by adding slowly the colloidal suspension of exfoliated titanium oxide nanosheets into the aqueous suspension of CdS at room temperature under vigorous stirring. The hybridization reaction was done at 60 °C for 3 h. The ratio of Cd/(Ti+Rh) was fixed to be 2.5. The brown-reddish precipitate was separated by centrifugation, washed thoroughly with deionized water, and dried in vacuum at 40 °C for 24 h.

Characterization: The crystal structures of the pristine $K_{0.8}Ti_{(5.2-x)/3}Li_{(0.8-x)/3}Rh_xO_4$ materials and CdS–$Ti_{(5.2-x)/6}Rh_{x/2}O_2$ nanohybrids were studied with powder XRD analysis (Rigaku, $\lambda = 1.5418$ Å, 25 °C). The chemical compositions of the CdS–$Ti_{(5.2-x)/6}Rh_{x/2}O_2$ nanohybrids were examined with ICP spectrometry (PerkinElmer Optima-4300 DV). The crystal morphologies and hybrid structures of the present materials were investigated with FE-SEM (Jeol JSM-6700F) and TEM (Jeol JEM-2100F). The elemental distributions of the present materials were probed with EDS–elemental mapping analysis with an energy-dispersive X-ray spectrometer equipped in FE-SEM machine.

The surface areas and pore structures of the present nanohybrids were studied with N_2 adsorption–desorption isotherms at liquid nitrogen temperature using Micromeritics ASAP 2020. Before the measurement, the materials were activated by degassing process at 150 °C for 7 h under vacuum. Diffuse reflectance UV–vis spectra of the present nanohybrids were measured with a Sinco S-4100 spectrometer using an integrating sphere and adopting $BaSO_4$ as a reference to determine their optical properties and band structures. The PL spectra and photoinduced PL decay of the CdS–$Ti_{(5.2-x)/6}Rh_{x/2}O_2$ nanohybrids and CdS QDs were measured using Hitachi F-4500 spectrometer, in which a nanosecond Nd-YAG laser (Continuum surelite II-10, 10 Hz, 5 ns FWHM pulse) was utilized. The total output power for the irradiation was measured with a laser power meter (Ophire-optronics Ltd., Nova, 10A-P-V2-SH), and the irradiated laser power was 250 mW at 355 nm. At every 5 min of irradiation, the emission spectra of the samples were monitored with a spectrofluorimeter. The electronic structure and local atomic arrangement of the present materials were investigated with XANES analysis at Ti K-edge, Rh K-edge, and Cd K-edge. The present XANES spectra were measured with the EXAFS facility installed at beam line 10C at the Pohang Light Source (PLS, Pohang, Korea), in which the voltage and current of synchrotron electron beam were 3 GeV and 300 mA, respectively. The XANES spectra were collected at room temperature from the thin layer of powder samples deposited on transparent adhesive tapes in a transmission mode using gas-ionization detectors. The energies of the obtained spectra were carefully calibrated by measuring the spectrum of Ti, Rh, or Cd metal simultaneously. The present XPS spectra were measured for a thin layer of the sample on highly conductive copper foil using a XPS spectrometer with a twin source of X-ray beams to depress the charging effect. All the XPS spectra were calibrated on the basis of the adventitious C 1s peak at 284.5 eV to rule out the spectral modification by the charging effect.

Photocatalytic Reaction Test: The photocatalytic activities of the present nanohybrids were examined by monitoring the H_2 generation from photocatalyst suspension in a Pyrex reaction cell. As a sacrificial agent for the photoreduction of water molecules, a mixed aqueous solution of 0.1 M Na_2S and 0.02 M Na_2SO_3 was adopted. Before the photoreactions, the photocatalyst suspension was bubbled with Ar gas for 10 min. The photocatalytic reaction was carried out with a Newport Xe lamp (300 W) using an optical cutoff filter ($\lambda > 420$ nm) to eliminate UV light and a water filter to remove IR radiation. The amount of H_2 gas generated was estimated with a gas chromatography (GC, Shimadzu GC-2014).

Supporting Information

Supporting Information is available from the Wiley Online Library or from the author.

Acknowledgements

[1] J. L. Gunjakar, T. W. Kim, H. N. Kim, I. Y. Kim, S.-J. Hwang, *J. Am. Chem. Soc.* **2011**, *4*, 4947.

[2] H. N. Kim, T. W. Kim, I. Y. Kim, S.-J. Hwang, *Adv. Funct. Mater.* **2011**, *21*, 3111.

[3] T. W. Kim, H.-W. Ha, M.-J. Paek, S.-H. Hyun, J.-H. Choy, S.-J. Hwang, *J. Mater. Chem.* **2010**, *20*, 3238.

[4] I. Tsuji, H. Kato, A. Kudo, *Chem. Mater.* **2006**, *18*, 1969.

[5] X. Zhou, B. Jin, L. Li, F. Peng, H. Wang, H. Yu, Y. Feng, *J. Mater. Chem.* **2012**, *22*, 17900.

[6] V. M. Daskalaki, M. Antoniadou, G. L. Puma, D. I. Kondarides, P. Lianos, *Environ. Sci. Technol.* **2010**, *44*, 7200.

[7] R. Peng, C. Lin, J. Baltrusaitis, C.-M. Wu, N. M. Dimitrijevic, T. Rajh, S. May, R. Koodali, *Phys. Chem. Chem. Phys.* **2014**, *16*, 2048.

[8] Y. Chen, L. Wang, G. Lu, X. Yao, L. Guo, *J. Mater. Chem.* **2011**, *21*, 5134.

[9] G. Li, L. Wu, F. Li, P. Xu, D. Zhang, H. Li, *Nanoscale* **2013**, *5*, 2118.

[10] H. Park, W. Choi, M. R. Hoffmann, *J. Mater. Chem.* **2008**, *18*, 2379.

[11] J. S. Jang, S. H. Choi, H. G. Kim, J. S. Lee, *J. Phys. Chem. C* **2008**, *112*, 17200.

[12] G.-S. Li, D.-Q. Zhang, J. C. Yu, *Environ. Sci. Technol.* **2009**, *43*, 7079.

[13] J. L. Gunjakar, I. Y. Kim, J. M. Lee, Y. K. Jo, S.-J. Hwang, *J. Phys. Chem. C* **2014**, *118*, 3847.

[14] M. Osada, T. Sasaki, *Adv. Mater.* **2012**, *24*, 210.

[15] R. Konta, T. Ishii, H. Kato, A. Kudo, *J. Phys. Chem. B* **2004**, *108*, 8992.

[16] S. Ida, N. Kim, E. Ertekin, S. Takenaka, T. Ishihara, *J. Am. Chem. Soc.* **2015**, *137*, 239.

[17] J. E. Huheey, E. A. Keiter, R. L. Keiter, *Inorganic Chemistry: Principles of Structure and Reactivity*, 4th ed., Harper Collins, NY, USA **1993**, pp. 116–117.

[18] R. Niishiro, R. Konta, H. Kato, W.-J. Chun, K. Asakura, A. Kudo, *J. Phys. Chem. C* **2007**, *111*, 17420.

[19] S. Chen, K. Kimura, *Chem. Lett.* **1999**, *3*, 233.

[20] S. J. Gregg, K. S. W. Sing, *Adsorption, Surface Area and Porosity*, Academic Press, London **1980**.

[21] I. Y. Kim, J. M. Lee, T. W. Kim, H. N. Kim, H.-I. Kim, W. Choi, S.-J. Hwang, *Small* **2012**, *8*, 1038.

[22] N. J. Hess, M. L. Balmer, B. C. Bunker, S. D. Conradson, *J. Solid State Chem.* **1997**, *129*, 206.

[23] S. G. Hur, D. H. Park, T. W. Kim, S.-J. Hwang, *Appl. Phys. Lett.* **2004**, *85*, 4130.

[24] I. Arcon, A. Tuel, A. Kodre, G. Martin, A. Barbier, *J. Synchrotron Radiat.* **2001**, *8*, 575.

[25] The present CdS–Ti$_{1.73}\square_{0.27}$O$_4$ nanocomposite shows somewhat lower photocatalytic activity for H$_2$ evolution than does the CdS–Ti$_{1.825}\square_{0.175}$O$_4$ nanocomposite in the previous report of ref. [2]. This result is interpreted as a result of the higher content of vacancy sites in the Ti$_{1.73}\square_{0.27}$O$_4$ nanosheet of the present nanocomposite compared with Ti$_{1.825}\square_{0.175}$O$_4$ nanosheet used in previously report. Since vacancy in titanate nanosheet can act as a recombination center for photoexcited electrons and holes, the higher concentration of vacancy leads to the depression of photocatalytic efficiency.

[26] L. Qi, J. Yu, M. Jaroniec, *Phys. Chem. Chem. Phys.* **2011**, *13*, 8915.

[27] Q. Li, B. Guo, J. Yu, J. Ran, B. Zhang, H. Yan, J. R. Gong, *J. Am. Chem. Soc.* **2011**, *133*, 10878.

[28] Q. Xiang, B. Cheng, J. Yu, *Angew. Chem. Int. Ed.* **2015**, *54*, 2.

[29] J. Wang, D. Nyago, J. P. Lewis, Z. Hong, A. Manivannan, M. Zhi, M. Li, N. Wu, *J. Am. Chem. Soc.* **2009**, *131*, 12290.

[30] C. Burda, Y. Lou, X. Chen, A. C. S. Samia, J. Stout, J. L. Gole, *Nano Lett.* **2003**, *3*, 1049.

[31] T. Sasaki, M. Watanabe, H. Hashizume, H. Yamada, H. Nakazawa, *J. Am. Chem. Soc.* **1996**, *118*, 8329.

[32] T. Sasaki, M. Watanabe, *J. Am. Chem. Soc.* **1998**, *120*, 4682.

[33] S. Chen, K. Kimura, *Chem. Lett.* **1999**, *3*, 233.